Colossal Enhancement of Atomic Force Response in van der Waals Materials Arising from Many-Body Electronic Correlations

Paul Hauseux,[1] Alberto Ambrosetti,[2] Stéphane P. A. Bordas,[1] and Alexandre Tkatchenko[3,*]
[1]*Department of Engineering, University of Luxembourg, L-4365 Esch-sur-Alzette, Luxembourg*
[2]*Dipartimento di Fisica e Astronomia, Università degli Studi di Padova, 35131 Padova, Italy*
[3]*Department of Physics and Materials Science, University of Luxembourg, L-1511 Luxembourg City, Luxembourg*

(Received 15 June 2021; accepted 28 January 2022; published 10 March 2022)

Understanding complex materials at different length scales requires reliably accounting for van der Waals (vdW) interactions, which stem from long-range electronic correlations. While the important role of many-body vdW interactions has been extensively documented for the stability of materials, much less is known about the coupling between vdW interactions and atomic forces. Here we analyze the Hessian force response matrix for a single and two vdW-coupled atomic chains to show that a many-body description of vdW interactions yields atomic force response magnitudes that exceed the expected pairwise decay by 3–5 orders of magnitude for a wide range of separations between perturbed and observed atoms. Similar findings are confirmed for carbon nanotubes, graphene, and delamination of graphene from a silicon substrate previously studied experimentally. This colossal force enhancement suggests implications for phonon spectra, free energies, interfacial adhesion, and collective dynamics in materials with many interacting atoms.

DOI: 10.1103/PhysRevLett.128.106101

Many phenomena in materials involve interactions between electrons and atomic lattices. Such interactions are the cornerstone of many-body physics in condensed matter and they contribute to quantum phenomena such as the temperature-dependence of the electrical conductivity in metals [1,2], Cooper-pair formation in superconductivity [3,4], thermalization and transport of charge carriers [5], and magnetic properties of molecules and materials [2]. The dimensionality, system size, and nature of interatomic interactions (strong or weak bonding) are critical aspects that influence the multitude of phenomena arising from the interplay between electrons and atomic lattices in materials. Electron–lattice interactions are also key in applications, including adhesion, cohesion [6], debonding [7], and fracture [8] in materials under different conditions such as irradiation [9], embrittlement [10], and to investigate the impact of defects [11] on material reliability.

While a comprehensive understanding of electron-phonon coupling effects has been achieved in condensed-matter physics [1,12,13], little is known about the interplay between nuclear displacements and electronic fluctuations at the scale of engineering materials [14,15]. Even when it is recognized that quantum-mechanical forces at the atomic scale are crucial to determine the mechanics of materials at the macroscopic scale, quantum physics and continuum mechanics models are developed independently. Quantum-mechanical methods are restricted to the modeling of small and well-ordered systems, whereas mechanical properties in mesoscopic and macroscopic engineering problems are routinely quantified resorting to pairwise (PW) potentials.

In this Letter, we study systems of one and two interacting carbynelike chains (see Fig. 1 for the explanation of the geometry and the atomic interaction model). We focus on the analysis of the atomistic Hessian matrix, which measures the force response on an atom resulting from a perturbation of itself (diagonal terms) or a different atom (off-diagonal terms). The Hessian matrix gives access to computing many response properties, such as phonon eigenvalues and eigenvectors and free energies. We find that a quantum many-body description of vdW interactions yields atomic force response magnitudes that exceed the expected pairwise decay by 3–5 orders of magnitude for a wide range of separations between the perturbed and the observed atom. This is in contrast to ratios between many-body and pairwise vdW interaction energies for fixed structures, which rarely exceed an order of magnitude [16]. Linear chains are analyzed in this study to facilitate physical insight into complex many-body mechanisms. However, our findings of intricate coupling mechanisms between phonons and collective electronic correlations are also confirmed here for carbon nanotubes, graphene, and experimentally studied delamination of graphene from a Si substrate [15]. Our study is motivated by experimental

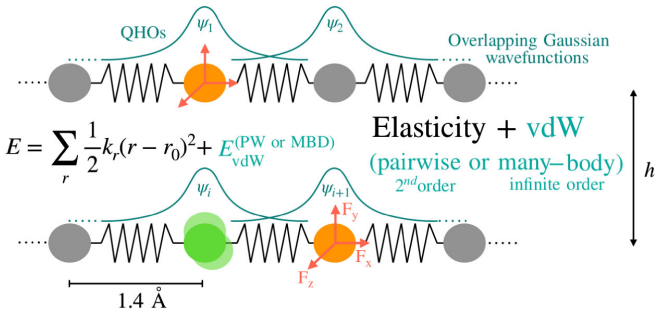

FIG. 1. Visual depiction of the studied geometry and the interatomic interaction model. Two carbyne chains with nearest-neighbor distance of 1.4 Å are separated by a vertical distance h. The vdW interactions between all atoms are treated via either a pairwise or a many-body model based on overlapping quantum harmonic oscillators coupled by a dipolar potential (see text for details). The Hessian matrix elements are computed analytically, measuring the force response at atom m (yellow atoms) to the displacement of atom n (green atom). For computing adhesive properties, the chemical bonds (local elasticity) are modeled via harmonic springs.

evidence of intriguing mechanical properties of systems at the nanometer and micrometer scales, due to their enhanced surface-to-volume ratio, high flexibility, and peculiar response properties [17–27]. The explanation of many of these experimental findings is expected to require accounting for many-body vdW correlation terms [16,28–32], and explicit inclusion of the complex geometrical distortions at the nanoscale [15].

We start by computing and analyzing the Hessian response matrix corresponding to pairwise (PW) and many-body vdW interactions. In what follows, we will use upper indices to refer to Cartesian $\{x, y, z\}$ components, lowercase lower indices to refer to atoms, and uppercase lower indices to indicate normal modes. The ath Cartesian component of the PW force acting on the ith atom is computed as

$$F_i^{\text{PW},a} = \partial_{r_i^a}\left(\sum_{j\neq i}^{N} f_{\text{damp}} \times C_{6,ij}/r_{ij}^6\right), \tag{1}$$

where $r_{ij} = |\mathbf{r}_i - \mathbf{r}_j|$ is the distance between atoms i and j, $C_{6,ij}$ is the vdW coefficient [33], and f_{damp} is a short-range damping function. Within the many-body dispersion (MBD) method, instead, the electronic response is mapped onto a set of atom-centered quantum harmonic oscillators (QHOs), coupled by a dipolar potential [34]. The interaction tensor $\boldsymbol{C}_{ij}^{\text{MBD},ab}$ is composed by N^2 (3×3) blocks that account for the coupling between each pair of atoms i and j:

$$\boldsymbol{C}_{ij}^{\text{MBD},ab} = \omega_i^2\delta_{ij}\delta_{ab} + (1-\delta_{ij})\omega_i\omega_j\sqrt{\alpha_i^0\alpha_j^0}\boldsymbol{T}_{ij}^{ab}. \tag{2}$$

Here α_i^0 and ω_i are the static dipole polarizability and characteristic frequency of the ith atom, while $\boldsymbol{T}_{ij}^{ab}$ is the dipolar tensor for two overlapping QHOs modeling atoms i and j. Diagonalization of the interaction tensor $\boldsymbol{S}^T\boldsymbol{C}^{\text{MBD}}\boldsymbol{S} = \boldsymbol{\Lambda}$ (where $\boldsymbol{\Lambda}_{IJ}^{ab} = \delta_{IJ}\delta_{ab}(\tilde{\omega}_I^a)^2$) yields the $3N$ collective oscillation modes of the system (via the transformation matrix $\boldsymbol{S}$) and the corresponding interacting frequencies $\tilde{\omega}_I^a$. The MBD interaction energy is computed as the QHO ground-state energy shift caused by the dipolar interaction

$$E_{c,\text{MBD}} = \hbar\left(\sum_{I=1}^{N}\sum_{a=\{x,y,z\}}\tilde{\omega}_I^a/2 - \sum_{j=1}^{N}3\omega_j/2\right). \tag{3}$$

The MBD atomic force acting on atom i, $F_i^{\text{MBD},a} = -\partial_{r_i^a}E_{c,\text{MBD}}$, can be written as

$$F_i^{\text{MBD},a} = -\frac{1}{4}[(\boldsymbol{\Lambda}_{JJ}^{bb})^{-1/2}\boldsymbol{S}_{Jl}^{Tbc}(\partial r_i^a\boldsymbol{C}^{\text{MBD}})_{lm}^{cd}\boldsymbol{S}_{mJ}^{db}], \tag{4}$$

where repeated indices are contracted (the same convention will be adopted hereafter). By definition, the MBD fluctuation modes have collective character, and this is reflected in the above force expression: Eq. (4) involves both dependence on *local* atomic indices (l, m) and *collective* degrees of freedom (MBD mode index J). The nonlocality of plasmon-like MBD modes implies that a change in the position (as well as mass and/or oscillator frequency) of a single atom could produce force response throughout the entire system.

To assess the relevance of the many-body mechanical response, we analyze the vdW Hessian tensor, defined as $\boldsymbol{H}_{ij}^{\text{MBD},ab} = -\partial r_i^a F_j^{\text{MBD},b}$ (with analogous expression for PW). This tensor quantifies the vdW force response on atom i, to an infinitesimal displacement of the atom j. The Hessian was computed analytically for both PW and MBD methods. Heat maps of the Hessian matrix for both PW and MBD interactions are plotted in Figs. 2(a) and 2(b). A system of two parallel chains is considered with 400 atoms per chain. In the presence of N atoms, the Hessian is a $3N\times 3N$ matrix. However, for our purposes it is sufficient to analyze the condensed Hessian $N\times N$ matrix $\boldsymbol{H}_{ij}^{*} = \sqrt{(\boldsymbol{H}_{ij}^{xx})^2 + (\boldsymbol{H}_{ij}^{yy})^2 + (\boldsymbol{H}_{ij}^{zz})^2}$. The off-diagonal Hessian components that couple longitudinal and transversal degrees of freedom are 5–6 orders of magnitude smaller and have no impact on the forthcoming analysis.

As expected, the displacement of an atom j has the largest impact on neighboring atoms i [see Figs. 2(a) and 2(b)]. Accordingly, largest Hessian elements are found on the main diagonal, measuring the force response at the atomic sites closest to the atomic perturbation within the same chain. The minor diagonal, instead, corresponds to the force response on the atoms belonging to the opposite chain (farther away due to finite interchain separation h). Comparison between MBD and PW results indicates a substantial role of many-body effects on the force-response nonlocality. Moreover, quasivanishing MBD Hessian elements found for long interatomic separations [darker

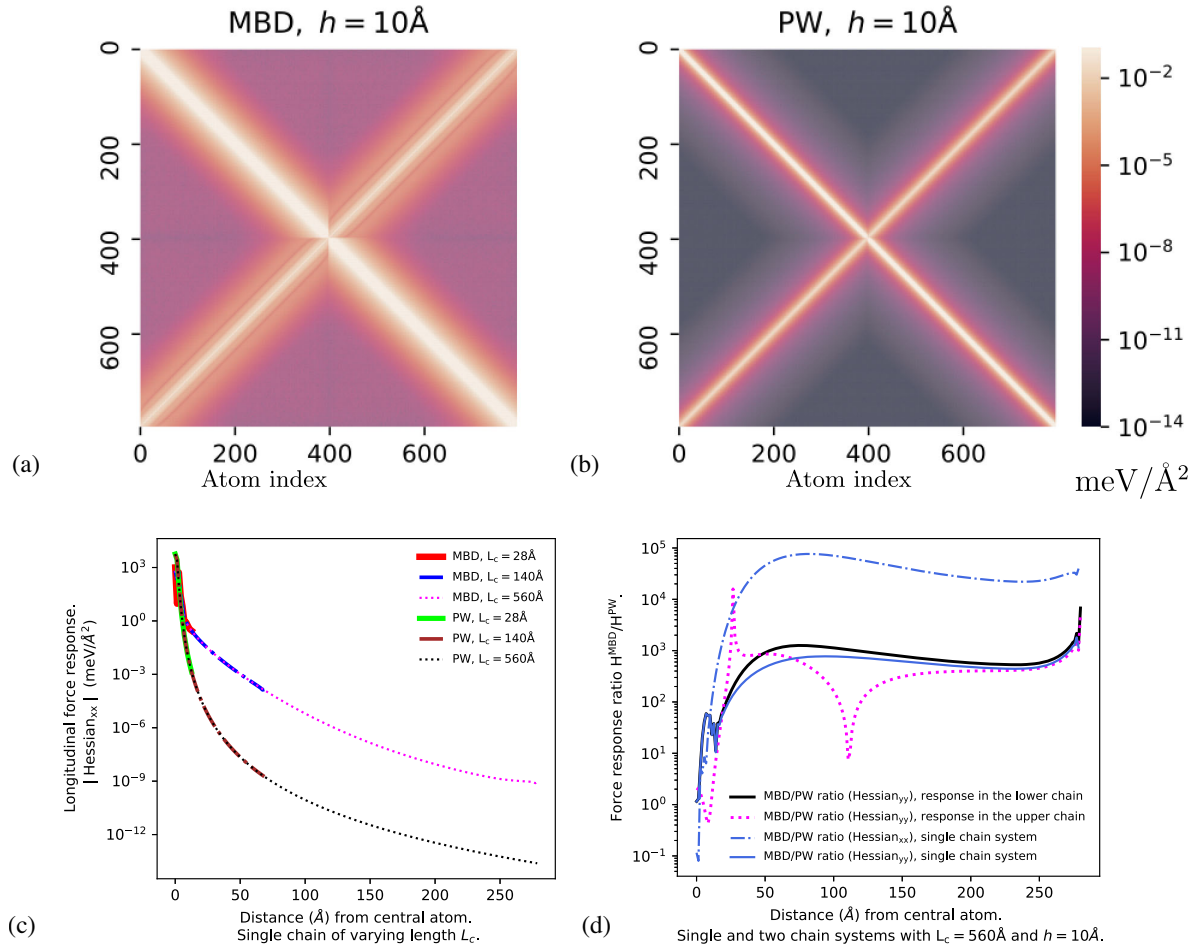

FIG. 2. Heat maps of the condensed Hessian matrix for (a) MBD and (b) PW vdW interactions. Plot axes in (a),(b) correspond to i and j atomic sites, respectively. A system of two parallel carbyne chains is considered (with 400 atoms per chain). Here $i, j = (1, 400)$ indicate atoms in the first chain, while $i, j = (401, 800)$ correspond to the second chain in reversed order. The main diagonal corresponds to force responses on the same chain, while the minor diagonal corresponds to the chain vertically separated by $h = 10$ Å. In panels (c) and (d), one-dimensional projections are shown upon longitudinal displacement of the central atom in one of the chains. Systems composed of one or two chains ($h = 10$ Å) with different lengths and different interchain distances were considered at MBD and PW levels.

regions in Figs. 2(a) and 2(b)] are about 3 orders of magnitude larger (10^{-9} meV/Å^2) than those found at the PW level (10^{-12} meV/Å^2). While both of these values may seem small, the substantial difference between MBD and PW has large implications for dynamics and adhesion as we will show below. We also suggest that long-range force response could play a key role at the macroscopic scale and ambient conditions, where the quantity of atoms approaches Avogadro's number and entropic effects always imply a certain degree of disorder at different interatomic length scales.

We now explicitly analyze the response in the longitudinal and transversal components of the atomic forces along the chain induced by a displacement of the central atom. As seen from Figs. 2(c) and 2(d), the MBD and PW force response acts along the chain in a radically different way. Within MBD, Hessian elements exhibit slower decay, and the MBD/PW ratio is always considerably greater than 1, in particular at long range with differences of 3–5 orders of magnitude.

Within the single chain we observe that, after a steep growth due to slower power law decay of the MBD interaction [16], the MBD/PW Hessian ratio tends to saturate [Fig. 2(d)] beyond the 70 Å scale. This is valid for both longitudinal and transversal Hessian components and suggests that MBD forces exhibit renormalized PW behavior at long range. The renormalization factor is very large, in fact it is necessary to multiply the PW C_6 parameter by $\sim 10^3$ and $\sim 10^5$ to effectively reproduce the transversal and longitudinal MBD results, respectively. Analogous renormalization effects occur also for interchain Hessian elements, i.e., for force perturbation due to atomic displacement in the other chain. In the transversal yy case, force response oscillations emerge along the chain. This can be analytically understood at the PW level, where a competition arises between a monotonically

decreasing R^{-8} factor (due to the second derivative of R^{-6}) and a term [proportional to $(7\Delta x^2 - h^2)/(\Delta x^2 + h^2)$, where $R^2 = h^2 + \Delta x^2$], which is increasing with x (longitudinal distance).

To rationalize the renormalized pairwiselike behavior of the MBD Hessian elements, we can rewrite the MBD energy in Eq. (3) using perturbative expansion in terms of the screened polarizability matrix $\boldsymbol{\mathcal{A}}_{ij}^{ab}$ and the coupling tensor $\boldsymbol{T}_{jm}^{bc}$ [34]:

$$E_{c,\mathrm{MBD}} \simeq -\int_0^\infty \frac{d\omega}{4\pi} \mathrm{Tr}[\boldsymbol{\mathcal{A}}_{ij}^{ab}(\mathrm{i}\omega)\boldsymbol{T}_{jm}^{bc}\boldsymbol{\mathcal{A}}_{mn}^{cd}(\mathrm{i}\omega)\boldsymbol{T}_{ni}^{da}]. \quad (5)$$

The shown second-order term scales as $\mathcal{C}_{6,jm} r_{jm}^{-6}$ with a screened $\mathcal{C}_{6,jm}$ coefficient and yields the exact MBD interaction energy for widely separated atoms j and m, while at shorter distances higher-order terms containing higher powers of $\boldsymbol{\mathcal{A}}$ and $\boldsymbol{T}$ should be considered. We computed the polarizability $\boldsymbol{\mathcal{A}}$ of the single chain using the self-consistent screening (SCS) equation [35,36]. The resulting matrix $\boldsymbol{\mathcal{A}}_{ij}^{ab}$ measures the dipolar response at site i to an electric field applied at j. From Fig. 3 we observe that the longitudinal (xx) polarizability is nonlocal, but has a finite range λ_C of around ~70 Å, due to the presence of a finite gap [16] in the dipole excitation spectrum. The renormalization of the single diagonal elements $\boldsymbol{\mathcal{A}}_{ii}^{xx}$ is moderate. However, due to the nonlocality of the total polarizability tensor given by off-diagonal elements, about 100 carbon atoms coherently polarize in the presence of a local electric field. The cumulative longitudinal dipole response of these atoms amounts to ~400 bohr^3, which

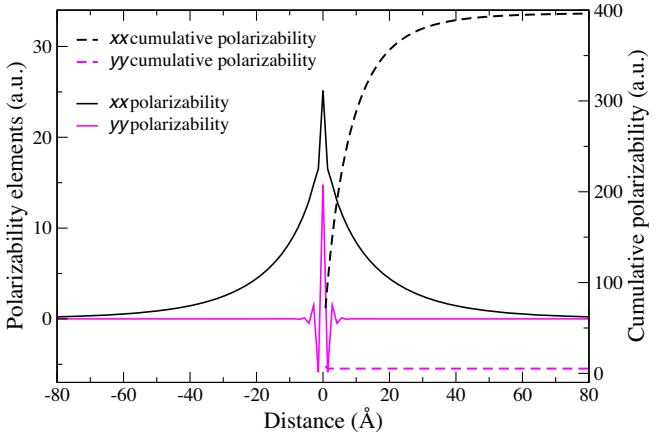

FIG. 3. Interacting polarizability for a carbyne chain containing 2001 atoms. Solid lines report polarizability elements $\boldsymbol{\mathcal{A}}_{ij}^{aa}$: the longitudinal ($a = x$) and transversal ($a = y$) dipole response measured at the atom j, located at a given distance from the central atom ($\bar{i} = 1001$), due to an electric field applied at $\bar{i}$. Negative distances represent the left side of the chain. Dashed lines correspond to the cumulative response (sum of all atomic xx or yy components, $\sum_j \boldsymbol{\mathcal{A}}_{ij}^{aa}$ over the entire chain).

corresponds to a polarizability renormalization factor of ~40 compared to an isolated carbon atom. This polarization enhancement is characteristic for Coulomb screening in low-dimensional systems, where electronic many-body effects imply strong and delocalized [16] polarization response in contrast to dense well-ordered solids [35]. The finite coherence length scale λ_C implies that for distances larger than λ_C, different chain fragments perceive each other as collective polarizability centers. In other words, the vdW interaction between atoms i and j is amplified by the surrounding atoms within λ_C, which respond simultaneously, increasing the internal electric field response along the chain. We note that the C_6 coefficient for two identical oscillators having static polarizability α and oscillator frequency $\bar{\omega}$ is proportional to $\alpha^2\bar{\omega}$. Hence, by accounting for the polarizability of the coherent chain fragments (characterized by the rescaling factor ~40 and containing 100 atoms), one obtains an effective C_6 coefficient renormalization of ~10^3, which qualitatively accounts for our numerical observations in Fig. 2. The even larger renormalization (~10^5) found in the xx Hessian elements stems from charge-overlap effects, that are most sensitive to longitudinal displacements. In contrast, minor renormalization effects are observed in the transverse yy polarizability, while mixed xy terms are essentially vanishing. As shown in Fig. 3, the yy polarizability is far less nonlocal than xx, as a consequence of a rapidly damped oscillatory behavior, reminiscent of Friedel's oscillations [2].

In real materials, the geometry of collective polarizability centers will depend on two main factors: nonlocal electronic polarization and charge overlap effects. Low-dimensional and heterogeneous materials with complex unit cells are characterized by strongly nonlocal polarization response [16,30,31,35], thus we expect the colossal force enhancement to hold in general for materials of arbitrary dimensionality where polarizable covalent bonds (dense regions) interplay with van der Waals interactions (sparse regions). For example, 3D organic–inorganic frameworks exhibit strong MBD interactions [37], and should in turn possess colossal atomic force response. In contrast, minor effects are expected for solids with small unit cells where the polarization response is effectively localized or for materials with small dielectric constants such as noble-gas solids. To show that our findings for chains can be generalized to more complex structures, we carried out Hessian calculations for a graphene layer and a carbon nanotube. In both cases, we find renormalization factors $\boldsymbol{H}^{\mathrm{MBD}}/\boldsymbol{H}^{\mathrm{PW}}$ of 10^3 to 10^4 at large interatomic separations, thus confirming the general relevance of colossal force response in vdW materials (see Supplemental Material [38] for a detailed analysis).

Finally, we demonstrate the importance of the many-body force response for adhesive interactions between two (initially parallel) carbyne chains. We use a hybrid

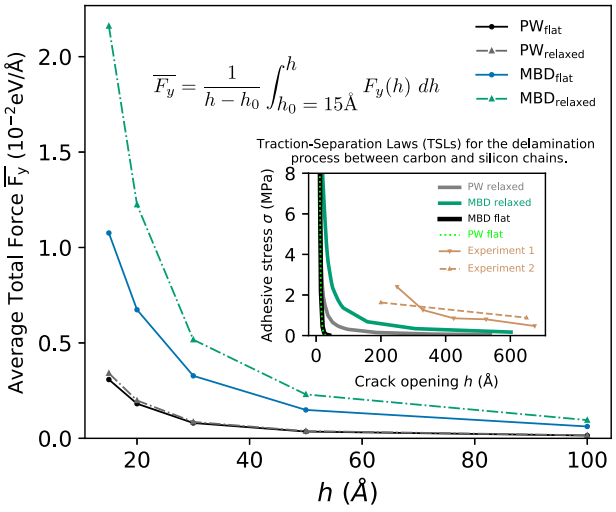

FIG. 4. Average vdW transverse force, defined by the given formula, acting on the lower chain as a function of separation distance h in flat and relaxed geometries. Upon geometry optimization, PW and MBD forces radically differ, especially at small and medium distances, where the MBD/PW ratio difference is highest. Inset: Traction-separation for the delamination of two initially parallel C and Si chains (see Ref. [15] and the Supplemental Material [38] for more detail). Experimental data [39] for the delamination of a graphene layer from a Si substrate are shown.

approach introduced in Ref. [15] that combines classical elasticity for local chemical bonding and nonlocal vdW interactions to compute vertical adhesive forces (see Fig. 1 for the depiction of the two-chain model). We compare in Fig. 4 the average vdW force acting on the lower chain for two different cases: flat (unrelaxed) configuration and fully relaxed geometry obtained starting from flat parallel configuration constraining edge atoms to their initial positions, at different edge-edge interchain distances h. For a set of h values starting from $h_0 = 15$ Å, we first compute the total vdW force F_y acting on the lower chain and then compute the average force $\bar{F}_y$ as defined in Fig. 4. The inclusion of MBD interactions consistently leads to stronger adhesive forces compared to the PW method. The two chains slightly bend upon relaxation, effectively reducing the interchain separation, and the effect is larger when the MBD method is used. For instance, the average and minimum MBD (PW) interchain separations are 19.75 (19.96) and 19.63 Å (19.94 Å), respectively, when $h = 20$ Å. In addition, geometry relaxation using PW vdW forces leads to a negligible change in the adhesion, while relaxed geometries with MBD yields an increase of a factor of 2 in the adhesive force. We note that much larger adhesive force enhancements are observed upon delamination of two ~ 2 μm long coupled chains (see Fig. 1 inset, and Ref. [15]). The two chains (initially parallel, and composed of C and Si atoms, respectively) were withdrawn from each other, opening a crack of width h from the left edge and measuring the mechanical stress as a function of h. Qualitatively different traction-separation laws are found after geometrical relaxation comparing MBD and PW models, not only in terms of higher stress modulus, but also of much longer range obtained with MBD. The force response in vdW materials arising from many-body electronic correlations is responsible for this enhancement effect, and explains the micrometer-scale adhesive stress observed in experiments [15,25,26,39]. In fact, even longer-ranged stress was found when going from 1D chains to more appropriate 2D/3D delamination models [15], providing qualitative agreement with experimental data.

In summary, we found a cooperative interplay between electronic correlations and atomic force response in materials coupled by van der Waals interactions. The nonlocal electronic polarization response and the quantum-mechanical treatment of vdW interactions beyond PW approximations are crucial to correctly describe this collective effect. The emergent force response drives nontrivial geometrical relaxations [15] in qualitative agreement with the experimental evidence of micrometer-ranged stress upon graphene delamination. Many material properties stem from the atomic Hessian matrix, meaning that our findings may have implications for phonon spectra, free energies, interfacial adhesion, and in general collective dynamics in materials possessing both dense and sparse regions.

We are grateful for the support of the Fonds National de la Recherche Luxembourg Grant No. O17-QCCAAS-11758809. The calculations presented in this Letter were carried out using the HPC facilities of the University of Luxembourg. A. A. acknowledges funding from Cassa di Risparmio di Padova e Rovigo (CARIPARO)—grants EngvdW and Synergy. A. T. acknowledges financial support by the European Research Council (ERC-CoG grant BeStMo). S. P. A. B. thanks the support of the European Union Horizon 2020 research and innovation programme TWINNING Project DRIVEN https://2020driven.uni.lu under Grant Agreement No. 811099.

P. H. and A. A. contributed equally to this work.

*alexandre.tkatchenko@uni.lu

[1] F. Giustino, Electron-phonon interactions from first principles, Rev. Mod. Phys. **89**, 015003 (2017).
[2] N. W. Ashcroft and N. D. Mermin, *Solid State Physics*, HRW international editions (Holt, Rinehart and Winston, New York, U.S.A., 1976).
[3] S. Y. Savrasov and D. Y. Savrasov, Electron-phonon interactions and related physical properties of metals from linear-response theory, Phys. Rev. B **54**, 16487 (1996).
[4] L. N. Cooper, Bound electron pairs in a degenerate Fermi gas, Phys. Rev. **104**, 1189 (1956).
[5] S. Dal Forno and J. Lischner, Electron-phonon coupling and hot electron thermalization in titanium nitride, Phys. Rev. Mater. **3**, 115203 (2019).

[6] L. Guin, J. L. Raphanel, and J. W. Kysar, Atomistically derived cohesive zone model of intergranular fracture in polycrystalline graphene, J. Appl. Phys. **119**, 245107 (2016).
[7] K. Gall, M. F. Horstemeyer, M. Van Schilfgaarde, and M. I. Baskes, Atomistic simulations on the tensile debonding of an aluminum–silicon interface, J. Mech. Phys. Solids **48**, 2183 (2000).
[8] M. Xu, A. Tabarraei, J. T. Paci, J. Oswald, and T. Belytschko, A coupled quantum/continuum mechanics study of graphene fracture, Int. J. Fract. **173**, 163 (2012).
[9] S. Serebrinsky, E. A. Carter, and M. Ortiz, A quantum-mechanically informed continuum model of hydrogen embrittlement, J. Mech. Phys. Solids **52**, 2403 (2004).
[10] O. Barrera, D. Bombac, Y. Chen, T. D. Daff, E. Galindo-Nava, P. Gong, D. Haley, R. Horton, I. Katzarov, J. R. Kermode *et al.*, Understanding and mitigating hydrogen embrittlement of steels: A review of experimental, modelling and design progress from atomistic to continuum, J. Mater. Sci. **53**, 6251 (2018).
[11] R. Khare, S. L. Mielke, J. T. Paci, S. Zhang, R. Ballarini, G. C. Schatz, and T. Belytschko, Coupled quantum mechanical/molecular mechanical modeling of the fracture of defective carbon nanotubes and graphene sheets, Phys. Rev. B **75**, 075412 (2007).
[12] P. Hofmann, I. Y. Sklyadneva, E. D. L. Rienks, and E. V. Chulkov, Electron-phonon coupling at surfaces and interfaces, New J. Phys. **11**, 125005 (2009).
[13] L. Pintschovius, Electron-phonon coupling effects explored by inelastic neutron scattering, Phys. Stat. Solids B **242**, 30 (2004).
[14] W. A. Curtin and R. E. Miller, Atomistic/continuum coupling in computational materials science, Model. Simul. Mater. Sci. Eng. **11**, R33 (2003).
[15] P. Hauseux, T.-T. Nguyen, A. Ambrosetti, K. Saleme Ruiz, S. P. A. Bordas, and A. Tkatchenko, From quantum to continuum mechanics in the delamination of atomically-thin layers from substrates, Nat. Commun. **11**, 1651 (2020).
[16] A. Ambrosetti, N. Ferri, R. A. DiStasio Jr., and A. Tkatchenko, Wavelike charge density fluctuations and van der Waals interactions at the nanoscale, Science **351**, 1171 (2016).
[17] K. S. Novoselov, A. K. Geim, S. V. Morozov, D. Jiang, M. I. Katsnelson, I. V. Grigorieva, S. V. Dubonos, and A. A. Firsov, Two-dimensional gas of massless Dirac fermions in graphene, Nature (London) **438**, 197 (2005).
[18] Y. Zhang, Y. W. Tan, H. L. Stormer, and P. Kim, Experimental observation of the quantum hall effect and Berry's phase in graphene, Nature (London) **438**, 201 (2005).
[19] A. A. Balandin, S. Ghosh, W. Bao, I. Calizo, D. Teweldebrhan, F. Miao, and C. N. Lau, Superior thermal conductivity of single-layer graphene, Nano Lett. **8**, 902 (2008).
[20] C. Lee, X. Wei, J. W. Kysar, and J. Hone, Measurement of the elastic properties and intrinsic strength of monolayer graphene, Science **321**, 385 (2008).
[21] S. Xie, L. Tu, Y. Han, L. Huang, K. Kang, K. U. Lao, P. Poddar, C. Park, D. A. Muller, R. A. DiStasio Jr., and J. Park, Coherent, atomically thin transition-metal dichalcogenide superlattices with engineered strain, Science **359**, 1131 (2018).
[22] A. Ambrosetti and P. L. Silvestrelli, Faraday-like screening by two-dimensional nanomaterials: A scale-dependent tunable effect, J. Phys. Chem. Lett. **10**, 2044 (2019).
[23] S. R. Na, J. W. Suk, L. Tao, D. Akinwande, R. S. Ruoff, R. Huang, and K. M. Liechti, Selective mechanical transfer of graphene from seed copper foil using rate effects, ACS Nano **9**, 1325 (2015).
[24] S. R. Na, S. Rahimi, L. Tao, H. Chou, S. K. Ameri, D. Akinwande, and K. M. Liechti, Clean graphene interfaces by selective dry transfer for large area silicon integration, Nanoscale **8**, 7523 (2016).
[25] H. Xin, R. Borduin, W. Jiang, K. M. Liechti, and W. Li, Adhesion energy of as-grown graphene on copper foil with a blister test, Carbon **123**, 243 (2017).
[26] S. R. Na, D. A. Sarceno, and K. M. Liechti, Ultra long-range interactions between silicon surfaces, Int. J. Solids Struct. **80**, 168 (2016).
[27] P. Loskill, H. Hähl, T. Faidt, S. Grandthyll, F. Müller, and K. Jacobs, Is adhesion superficial? Silicon wafers as a model system to study van der Waals interactions, Adv. Colloid Interface Sci. **179**, 107 (2012).
[28] J. F. Dobson, A. White, and A. Rubio, Asymptotics of the Dispersion Interaction: Analytic Benchmarks for van der Waals Energy Functionals, Phys. Rev. Lett. **96**, 073201 (2006).
[29] J. F. Dobson, Unusual features of the dispersion force in layered and striated nanostructures, Surf. Sci. **601**, 5667 (2007).
[30] J. F. Dobson and T. Gould, Calculation of dispersion energies, J. Phys. Condens. Matter **24**, 073201 (2012).
[31] A. Ambrosetti, P. L. Silvestrelli, and A. Tkatchenko, Physical adsorption at the nanoscale: Towards controllable scaling of the substrate-adsorbate van der Waals interaction, Phys. Rev. B **95**, 235417 (2017).
[32] J. Sarabadani, A. Naji, R. Asgari, and R. Podgornik, Many-body effects in the van der Waals–Casimir interaction between graphene layers, Phys. Rev. B **84**, 155407 (2011).
[33] A. Tkatchenko and M. Scheffler, Accurate Molecular Van Der Waals Interactions from Ground-State Electron Density and Free-Atom Reference Data, Phys. Rev. Lett. **102**, 073005 (2009).
[34] A. Tkatchenko, A. Ambrosetti, and R. A. DiStasio Jr., Interatomic methods for the dispersion energy derived from the adiabatic connection fluctuation-dissipation theorem, J. Chem. Phys. **138**, 074106 (2013).
[35] A. Tkatchenko, R. A. DiStasio Jr., R. Car, and M. Scheffler, Accurate and Efficient Method for Many-Body van der Waals Interactions, Phys. Rev. Lett. **108**, 236402 (2012).
[36] A. Ambrosetti, A. M. Reilly, R. A. DiStasio Jr., and A. Tkatchenko, Long-range correlation energy calculated from coupled atomic response functions, J. Chem. Phys. **140**, 18A508 (2014).
[37] X. Liu, J. Hermann, and A. Tkatchenko, Communication: Many-body stabilization of non-covalent interactions: Structure, stability, and mechanics of Ag3Co(CN)6 framework, J. Chem. Phys. **145**, 241101 (2016).
[38] See Supplemental Material at http://link.aps.org/supplemental/10.1103/PhysRevLett.128.106101 for detailed analysis of Hessian calculations for a graphene layer and a carbon nanotube, as well as additional results for graphene delamination from silicon substrate.
[39] S. R. Na, J. W. Suk, R. S. Ruoff, R. Huang, and K. M. Liechti, Ultra long-range interactions between large area graphene and silicon, ACS Nano **8**, 11234 (2014).